Available online at www.sciencedirect.com

ScienceDirect

Acta Materialia 81 (2014) 386–400

Acta MATERIALIA

www.elsevier.com/locate/actamat

Integrated experimental–simulation analysis of stress and strain partitioning in multiphase alloys

C.C. Tasan *, M. Diehl, D. Yan, C. Zambaldi, P. Shanthraj, F. Roters, D. Raabe

Max-Planck-Institut für Eisenforschung, Max-Planck-Straße 1, 40237 Düsseldorf, Germany

Received 4 April 2014; received in revised form 15 July 2014; accepted 31 July 2014

Abstract

The mechanical response of multiphase alloys is governed by the microscopic strain and stress partitioning behavior among microstructural constituents. However, due to limitations in the characterization of the partitioning that takes place at the submicron scale, microstructure optimization of such alloys is typically based on evaluating the averaged response, referring to, for example, macroscopic stress–strain curves. Here, a novel experimental–numerical methodology is introduced to strengthen the integrated understanding of the microstructure and mechanical properties of these alloys, enabling joint analyses of deformation-induced evolution of the microstructure, and the strain and stress distribution therein, down to submicron resolution. From the experiments, deformation-induced evolution of (i) the microstructure, and (ii) the local strain distribution are concurrently captured, employing in situ secondary electron imaging and electron backscatter diffraction (EBSD) (for the former), and microscopic-digital image correlation (for the latter). From the simulations, local strain as well as stress distributions are revealed, through 2-D full-field crystal plasticity (CP) simulations conducted with an advanced spectral solver suitable for heterogeneous materials. The simulated model is designed directly from the initial EBSD measurements, and the phase properties are obtained by additional inverse CP simulations of nanoindentation experiments carried out on the original microstructure. The experiments and simulations demonstrate good correlation in the proof-of-principle study conducted here on a martensite–ferrite dual-phase steel, and deviations are discussed in terms of limitations of the techniques involved. Overall, the presented integrated computational materials engineering approach provides a vast amount of well-correlated structural and mechanical data that enhance our understanding as well as the design capabilities of multiphase alloys.

Keywords: In situ testing; Digital image correlation; Crystal plasticity; Spectral method; Dual-phase steel

1. Introduction

Simultaneous improvement of material strength and ductility is achievable by microstructures that combine several deformation and strengthening mechanisms. With the exception of single-phase materials showing deformation-dependent transitions between different strain-hardening mechanisms (*e.g.* twinning-induced plasticity (TWIP) steels [1]), in current alloy design practice joint strength and ductility optimization is typically realized by introducing different phases with contrasting mechanical characteristics. Recent examples of such systems are dual-phase (DP, [2,3]), transformation-induced plasticity (TRIP, [4,5]) steels, and $(\alpha + \beta)$-Ti-alloys [6,7], etc.

The phase-specific deformation or transformation mechanisms present in such microstructures are triggered at different local stress or strain levels, and, therefore, the global performance of such alloys under mechanical loading critically depends on the evolution of stress and strain partitioning among the different phases. Thus, to understand the behavior of existing high-strength alloys and to

* Corresponding author. Tel.: +49 211 6792 866; fax: +49 211 6792 333.
E-mail address: c.tasan@mpie.de (C.C. Tasan).

http://dx.doi.org/10.1016/j.actamat.2014.07.071
1359-6454/

design new composites, phases and interfaces with improved properties, analysis of the microstructural strain and stress partitioning is crucial [8]. Moreover, to identify physically based microstructure design guidelines, it is essential that the measurement of strain and stress fields is further coupled to the measurement of the deformation-induced evolution of the underlying microstructure itself. The concurrent mapping of strain, stress and microstructure-evolution, however, is highly challenging since:

i. mapping of the deformation-induced evolution of such complex microstructures requires the use of microscopy techniques that provide excellent phase and defect contrast at both high resolution and large field of view;
ii. mapping of microscopic strain fields requires a high-performance microscopic-digital image correlation (μDIC) methodology that does not suffer from limited resolution/field-of-view, patterning-induced microstructure modification, and inaccuracies at high strain levels [9–14];
iii. mapping of microscopic stress fields at the required spatial resolution is challenging by stand-alone experiments, calling for complementary crystal mechanics simulations.

In the literature, the mapping of these three different "fields" has typically been achieved through experimental in situ techniques (e.g. [1,3,4,15–18]) or by numerical simulations [19–23], in an uncoupled manner. Among the experimental approaches, earlier works focused on basic mapping of microstructure evolution (based on topographic trace analysis) without strain mapping [16] or subsequently on mapping macroscopic strain fields without coupling to the underlying microstructure evolution [17,24]. Most recent efforts following the introduction of μDIC include mapping of microscopic strain fields together with some basic (*i.e.* topography-based) analysis of microstructure evolution [14,15,25,26]. A more direct coupling between μDIC and the underlying microstructure is obtained through accompanying electron backscatter diffraction (EBSD) measurements in Ref. [27]. Among the simulation efforts, the great majority of early works were based on morphologically simplified unit cell models [20,22,23,28]. In the recent years, crystal plasticity (CP) finite-element method (FEM)-based numerical analyses were increasingly based on experimentally obtained microstructure maps [19,29–38]. This trend is expected to further develop and include an increasing level of microstructural authenticity and detail (e.g. [37,38]). There are, however, only few very recent examples [39,40] that aim to couple the deformation-induced microscopic strain or stress field evolution to the experimental analysis of the deformation of the same starting microstructure. A number of technical challenges have hampered the interactions between experiments and simulations so far, and thus more holistic approaches to couple advanced experimental and simulation tools and methodologies in an integrated manner are required to match the three requirements (i)–(iii) described above.

In this work we present a novel, integrated experimental–numerical methodology that fulfills these conditions, allowing concurrent analysis of deformation-induced evolution of microstructure, strain partitioning and stress partitioning. With this methodology, as shown schematically in Fig. 1, the first is derived from experiments and the last from the corresponding CP simulations, while the strain mapping is obtained from both. In the experiments, to allow strain and microstructure mapping (*i.e.* challenges (i) and (ii) above), a recently developed μDIC technique is employed that provides high-resolution (approximately 0.1 ± 0.001 μm) strain maps without inhibiting the application of EBSD measurements, electron channeling contrast imaging (ECCI) [41] and secondary electron (SE) imaging measurements of the same microstructural region [10]. The simulation route also starts from the EBSD map of the same area (Fig. 1), from which a crystallographically informed numerical model is created with phase properties obtained from inverse CPFEM simulations of nanoindentation experiments [42,43]. Using a recently developed spectral solver suitable for heterogeneous materials with high mechanical phase contrast and nonlinear stress–strain response [44,45], full-field CP simulations are carried out. Guided by a comparison with the experimentally obtained strain fields, these simulations allow mapping local stress fields, thus providing an indirect solution for challenge (iii) described above.

Here we demonstrate the potential of the methodology on the example of a DP steel, which is an ideal case study material for stress and strain partitioning due to the coexistence of the high mechanical contrast phases martensite and ferrite with comparable volume fractions. First, a detailed explanation of the experimental and numerical methods is provided, followed by results obtained from both routes in a consecutive manner. These results are then analyzed and discussed in direct comparison, focusing on various phenomena that are characteristic for DP steel micromechanics.

2. Methodology

The strength of the methodology lies in the strong coupling between experiment and modeling as schematically outlined in Fig. 1. In this section, the methodologies followed in both routes are explained in detail, referring to Figs. 2 and 3, respectively.

2.1. In situ experiments

For the experiments, tensile samples with gauge dimensions of 4 mm × 2 mm × 1 mm are produced by spark erosion. Specimen surfaces are polished with colloidal SiO_2 particles ranging from 0.01 to 0.05 μm in size, following a conventional metallographic grinding, diamond polishing and etching procedure. Preliminary large field-of-view

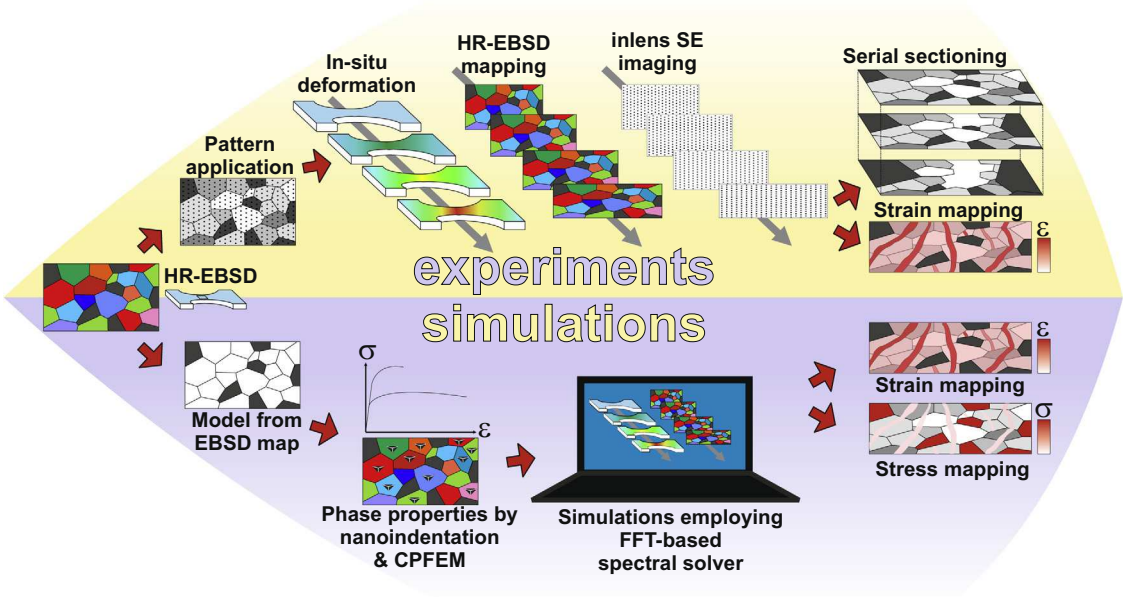

Fig. 1. The integrated approach involves experiments and simulations both proceeding from the same EBSD-mapped microstructure data sets, providing the deformation-induced local strain and stress distribution maps as well as the associated microstructural changes. Note that the schematic descriptions of the obtained strain maps here represent the ideal case, whereas differences unavoidably exist between experimentally and numerically obtained maps.

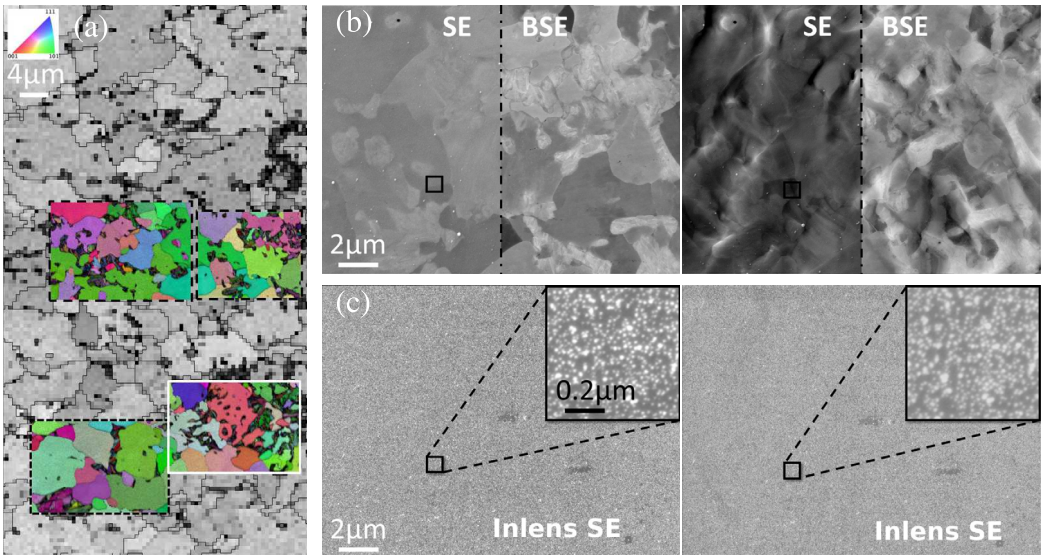

Fig. 2. Methodology of region of interest (ROI) selection and microstructure imaging during the deformation experiments: (a) EBSD-based IQ map that shows the locations of the ROIs with high-resolution IPF overlays. The ROI with the solid white border is discussed in detail in this paper, whereas the upper and lower left ROIs are discussed elsewhere [46]. (b) BSE/SE microstructure images at the undeformed state (left) and at $\bar{\varepsilon}_x = 0.08$ strain in the horizontal loading direction (right). (c) In-lens SE microstructure images at undeformed state (left) and at $\bar{\varepsilon}_x = 0.08$ strain in the horizontal loading direction (right). High-magnification insets show that microstructure-free pattern images are obtained by the in-lens detector. Note that all images in (b) and (c) are of exactly the same ROI, underlining the strength of the developed selective pattern imaging methodology.

EBSD measurements are conducted to identify regions of interest (ROIs) that enable a comparison of the influence of different microstructural features on strain partitioning (Fig. 2a). In the case of DP steel considered here, the influence of ferrite grain size, martensite fraction, martensite distribution, etc., can be investigated with this approach that benefits from the inherent microstructural heterogeneity. EBSD measurements and scanning electron microscopy (SEM) imaging are carried out using a Zeiss-Crossbeam XB 1540 focused ion beam (FIB)-SEM instrument (Oberkochen, Germany). This instrument is also equipped with an EDAX/TSL system (Draper UT, USA). For the high spatial resolution EBSD images of the chosen ROIs in Fig. 2a an acceleration voltage of 15 kV with a step size of 100 nm was chosen. Pattern quality and misorientation distributions obtained in the EBSD measurements confirm

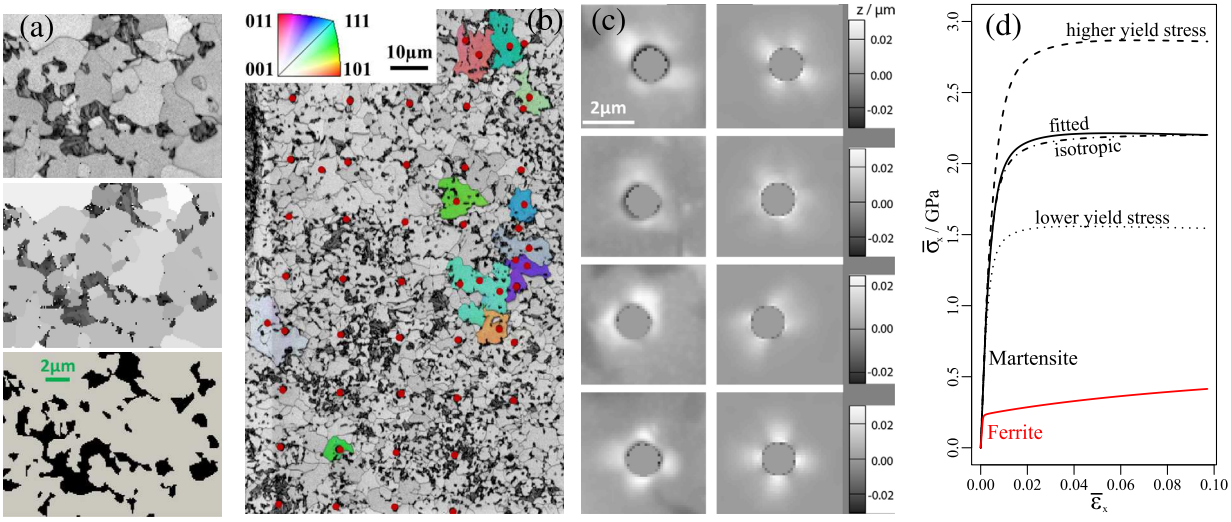

Fig. 3. The model for the CP simulations is based on the real microstructure as shown in (a), where the three images show the EBSD-based image quality (IQ) map (top), EBSD grain average IQ (GavgIQ) maps (middle) and the resulting phase map (bottom). Phase properties are extracted from nanoindentation experiments, AFM measurements and follow-up CPFEM simulations as shown in (b)–(d). Note that in (b), indent locations are highlighted by red dots, and orientations of considered grains (IPF shown in inset parallel to normal direction); in (c), the AFM measured pile-up topography of these indents are provided (left) together with simulated topographies (right); and in (d), determined ferrite phase behavior is presented together with the different martensite behaviors considered. (For interpretation of the references to colour in this figure legend, the reader is referred to the web version of this article.)

deformation-free surface preparation obtained by the aforementioned procedure.

Prior to the deformation experiments, a single layer of 0.015 ± 0.005 μm SiO_2 particles is homogeneously distributed on the sample surfaces for follow-up local strain field measurements. More details on this procedure are given in Ref. [10]. As shown in Fig. 2, the single layer pattern of SiO_2 particles offers two distinct advantages. On the one hand, it does not obstruct imaging of surface topography (by SE imaging) and the underlying microstructure (by backscatter electron (BSE) imaging) as demonstrated in Fig. 2b, thus allowing microstructure imaging without any interference from the overlaying pattern. On the other hand, the SiO_2 pattern can be selectively imaged for μDIC at high resolution without any disturbance by the underlying microstructure (thus avoiding effects of surface roughening and/or changing electron channeling conditions) by in-lens SE imaging as shown in Fig. 2c.

Next, using a KAMMRATH & WEISS (Dortmund, Germany) stage, the tensile sample is deformed in uniaxial tension to increasing levels of strain. At each deformation level, ROIs are imaged using different SEM detectors (*i.e.* SE, BSE, in-lens SE, EBSD). The images captured by the in-lens SE detector are used for the μDIC analysis using the ARAMIS software (GOM GmbH, Braunschweig, Germany). For optimal image correlation and microstructure imaging, small interaction volume (low-kV) imaging conditions are employed and images of (at least) 2048 pixel × 1536 pixel resolution are taken.

Following the deformation experiments, a colloidal SiO_2 polishing based serial sectioning procedure is carried out to reveal the 3-D microstructure underneath the observed surface layer. For precise positioning of the investigated area inside of each section, FIB-milled markers are placed in the sample surface, sufficiently away from the ROIs to avoid FIB damage. The geometry of the markers (*i.e.* triangular prism, whose triangular base is perpendicular to the specimen surface) are used to indicate the depth of sectioning. SE/BSE imaging and EBSD mapping are then conducted for selected depths, to reveal the phases below the surface topology in the ROIs.

2.2. Full-field crystal plasticity simulations

For establishing a physically based modeling approach on the basis of a high-fidelity microstructure mapping of the in situ experiments outlined above, a direct, *i.e.* mesh-free simulation of the probed microstructure patches is required. For this reason, the EBSD data obtained on the investigated microstructural areas (Fig. 2a) is set as the starting point for the CP simulations [47,48] using the DAMASK framework [49,50]. This framework can provide various constitutive models, *e.g.* a phenomenological description [51], a dislocation-based model (incorporating TWIP effects [52]), and a formulation taking dislocation flux into account [53]. For the proof-of-principle presented here, the phenomenological model (details are presented in Appendix A.1) was employed. In contrast to the more complex constitutive models, whose predictive capabilities heavily depend on—often experimentally not accessible—physical parameters, the phenomenological model can be fitted without ambiguities to the actual material properties as described further below in this section. As is shown later, it is encouraging in the context of the proposed method to

see that various important micromechanical phenomena can be already successfully captured using this rather simple model.

Handling the increased computational challenges associated with the underlying complex microstructures and the strong mechanical contrast among the phases present in DP steels requires an advanced numerical solution strategy that reaches beyond the established CPFEM approaches [54]. Efficiency requirements are also of specific importance for achieving longer-term goals of such integrated computational materials engineering (ICME) approaches, as in the case of full experimental calibration, multiple stand-alone simulations of artificial microstructural variants would be routinely run to systematically screen the influence of specific microstructural parameters. To this end, the authors have recently developed an advanced spectral method-based solver to replace the de facto standard FEM for solving the associated boundary value problems [44,45]. A short summary of the spectral method, which was originally proposed by Moulinec and Suquet [55,56] and has been well established in material mechanics for solving boundary value problems during the last decade [57–60], is given in Appendix B. More details of the used implementation can be found in Refs. [44,45]. The authors (among others) have recently demonstrated that this solver overcomes some limitations of the FEM, such as unfavorable scaling for large problems, the inability to capture high spatial gradients and the necessity of meshing [44]. The latter is achieved as the spectral method allows a direct use of the regular grid provided by the discrete EBSD points. Thus, each computation point is assigned a phase (*i.e.* martensite or ferrite, based on the grain average image quality (IQ), see Fig. 3a) and initial crystallographic orientation (Fig. 2a). Phase transformation is not included in the model. Since it is known from experimental observations that retained austenite transforms to martensite during the early deformation states in the material considered, austenitic grains are treated as martensite. The resulting phase distribution is shown in Fig. 3a for the ROI discussed herein.

Additional microstructural authenticity is introduced in the model by extracting the phase properties directly from the microstructure itself (Fig. 3b–d). This is done with the help of an inverse CPFEM simulation procedure which was originally developed for and applied to hexagonal materials [42,43,61]. As shown in Ref. [42] this procedure can serve as an substitute for single-crystal experiments with the significant advantage that chemical composition and heat treatment are exactly the same for "single-crystal" and polycrystal experiments. It is here applied to the case of the body-centered cubic crystal structure of ferrite. This approach to identify the mechanical behavior of the ferrite matrix phase involves optimization of initial and final resolved shear stress on the $\langle 111\rangle$ $\{110\}$ and $\langle 111\rangle$ $\{112\}$ slip system families in four differently oriented grains (Fig. 3c) to correctly predict the pile-up topography resulting from nanoindentation experiments (Fig. 3b). To achieve this, load-controlled indentation experiments ($F_{max} = 4.0$ mN) are performed using a spheroconical diamond tip with a nominal tip radius of 1.0 μm and a nominal cone angle of 90° on the same undeformed DP microstructure (away from the ROIs). From the array of indents, those in the center of differently oriented, large ferrite grains are selected (shown as highlighted grains in Fig. 3b). Thus, grain boundary effects on indentation measurements, and surface relief effects on follow-up atomic force microscopy (AFM) measurements are both minimized. The pile-up topography in the vicinity of the indents (10 mm × 10 mm) are measured using tapping-mode AFM measurements with a scan rate of 0.25 Hz and a tip velocity of 5 $\mu m s^{-1}$. Finally, using a NELDER–MEAD-type nonlinear optimization algorithm, the initial and saturation shear strength values for the two slip system families are identified. The objective function is based on differences in pile-up topographies (Fig. 3c) and the load–displacement curves. The identified set of parameters is given in Table 1a and shown in comparison to the martensite stress–strain curves in Fig. 3d. Employment of the DAMASK framework allows exactly the same material point model to be used for both the simulation of the periodically repeated DP microstructure with the fast and efficient spectral solver, and for the parameter identification procedure with the commercial FEM solver MSC.Marc.

As shown in Fig. 3c for the four chosen grains, the final CPFEM-predicted pile-up patterns are in good agreement

Table 1
Material parameters, based on Ref. [62] and adjusted to actual phase properties. (a) Ferrite, initial and saturation slip resistance determined using inverse simulation procedure. (b) Martensite, initial and saturation slip resistance fitted to stress–strain curve and hardness ratio.

Property	Value	Unit
(*a*)		
C_{11}	233.3e9	Pa
C_{12}	135.5e9	Pa
C_{44}	118.0e9	Pa
$\dot{\gamma}_0$	1e-3	$m\,s^{-1}$
$s_{0,\{1\ 1\ 1\}}$	95e6	Pa
$s_{\infty,\{1\ 1\ 1\}}$	222e6	Pa
$s_{0,\{1\ 1\ 2\}}$	96e6	Pa
$s_{\infty,\{1\ 1\ 2\}}$	412e6	Pa
h_0	1e9	Pa
$h_{\alpha\beta}$	1.	
n	20	
w	2.25	
(*b*)		
C_{11}	417.4e9	Pa
C_{12}	242.4e9	Pa
C_{44}	211.1e9	Pa
$\dot{\gamma}_0$	1e-3	$m\,s^{-1}$
$s_{0,\{1\ 1\ 1\}}$	406e6	Pa
$s_{\infty,\{1\ 1\ 1\}}$	873e6	Pa
$s_{0,\{1\ 1\ 2\}}$	457e6	Pa
$s_{\infty,\{1\ 1\ 2\}}$	971e6	Pa
h_0	563e9	Pa
$h_{\alpha\beta}$	1.	
n	20	
w	2.25	

with the AFM-based experimental measurements. This indicates that the hardening behavior is correctly described by the determined set of parameters. However, as the approach described in Ref. [61] does not strongly penalize deviations from the load–displacement curve, the force is underestimated by the simulation and reaches only the values of approximately 2.5 mN instead of the experimentally determined 4.0 mN (for the same indent depths).

The same procedure is not applicable to the martensitic phase, as the dimensions of the martensitic laths are of similar size as the nanoindents. Therefore, for the martensite, constitutive parameters are fitted to macroscopic, *i.e.* polycrystal stress–strain curves. However, to strengthen the correlation with the material at hand, the initial flow stress ratio between ferrite and martensite (identified from the nanoindentation experiments) is considered. This ratio is used as a basis to scale the initial and final shear stress on each slip system family in the martensite. Moreover, the sensitivity of the simulation results on the martensitic phase properties is studied with the aid of follow-up simulations using the modified mechanical contrast between ferrite and martensite. To this end, martensite variations are introduced by ±25% scaling of the initial and final shear stress on each slip system family. Also, the influence of martensite anisotropy is investigated by comparing the results of fully anisotropic CP simulations to results obtained using an isotropic (J_2) model for the martensite. More details on constitutive aspects of the used models are given in Appendix A. The stress–strain curves for all used parameters for martensite are shown in Fig. 3d.

Using the same strain rate as in the experiment, namely $6.0 \times 10^{-4}\,s^{-1}$, the microstructural patches are loaded under tensile strain for 170 s, reaching a final average strain of approximately $\bar{\varepsilon}_x = 0.08$. The out-of-plane direction of the 2-D slice is set to be stress-free to reflect the experimental situation of a free surface. As it is characteristic for the spectral method, the microstructure is periodically repeated in all three directions, *i.e.* the prescribed boundary conditions are volume/area averages. It will be shown later (Section 3) that the strain heterogeneity is influenced mainly by the immediate neighborhood of a given microstructural area, suggesting that the influence due to the artificial periodicity introduced by the boundary description is confined to a narrow zone (see also [46]). Nevertheless, to minimize this deviation further the simulated microstructural areas are kept larger than those tracked experimentally. The errors introduced through the mentioned uncertainties in phase determination and through the setting of phase properties are critically discussed in Section 4.

3. Results

The coupled experimental–numerical methodology is applied for all four regions shown in Fig. 2a. For the proof-of-principle assessment of the methodology and the comparative analyses conducted here, the focus is placed on the one highlighted by a solid line in Fig. 2a. The experimental–numerical analyses of the deformation in the other ROIs are discussed elsewhere [46].

3.1. In situ experiments

The images obtained at different deformation stages (local average strain in horizontal loading direction $\bar{\varepsilon}_x = 0.00, 0.05, 0.08$) are presented in Fig. 4. The SE images (Fig. 4a), the μDIC maps (Fig. 4b) and the EBSD maps (Fig. 4d and c) clearly demonstrate that the developed experimental methodology [10] enables strain and microstructure mapping at an optimal combination of spatial resolution and field-of-view.

In the SE images presented in Fig. 4a, it is observed that deformation leads expectedly to significant surface roughening, arising from slip steps, grain rotations, grain sink-in, and damage incidents [47]. The heterogeneity of deformation observed here is clearly linked to the DP martensite–ferrite microstructure shown in the leftmost image in Fig. 4b. This figure is divided by dashed lines into four regions for the follow-up discussion. The trend in roughening observed up to $\bar{\varepsilon}_x = 0.05$ is preserved to $\bar{\varepsilon}_x = 0.08$ (Fig. 4a), suggesting that strain is heterogeneously distributed, but this distribution does not significantly change with increasing loading level. Local VON MISES strain maps in Fig. 4b, where the strain is overlaid on the EBSD high-angle (*i.e.* more than 15°) grain boundary map of only ferrite, confirm this observation. At an average strain of $\bar{\varepsilon}_x = 0.05$, there is already significant partitioning of strain between ferrite and martensite, such that the ferrite takes the majority of the plastic strain. The extent of strain partitioning among ferrite and martensite is also shown quantitatively in Fig. 5a. More interestingly, there is also strong partitioning among the ferritic regions (see, *e.g.* strain levels in region (ii) vs. region (iv) in the rightmost image in Fig. 4b and the scatter in VON MISES strain in ferrite regions in Fig. 5a). In fact, plastic strain is observed to be exceedingly high in submicron thick bands which are 45° to 50° oriented with respect to the loading direction. Such sharp deformation gradients are observed even within single ferritic grains (see region (iv) in rightmost image in Fig. 4b). In many cases, localization bands develop at the center of ferrite grains away from grain boundaries, and are aligned towards gaps between the surrounding martensite islands. With an increase in overall strain to $\bar{\varepsilon}_x = 0.08$, the local strain within the deformation bands increases further (up to an equivalent strain of approximately $\varepsilon_{vM} = 0.40$), while no new bands appear and the rest of the microstructure deforms relatively more sluggish. Clear damage incidents are also captured, as seen in the rightmost image in Fig. 4a. Most damage incidents are located in those boundary regions that separate the severely deformed regions (e.g. localization bands) from regions that are not significantly strained (e.g. martensitic zones).

In Fig. 4c, EBSD kernel average misorientation (KAM) maps are overlayed on EBSD high-angle (*i.e.* more than 15°) boundary maps of ferrite grains. The local

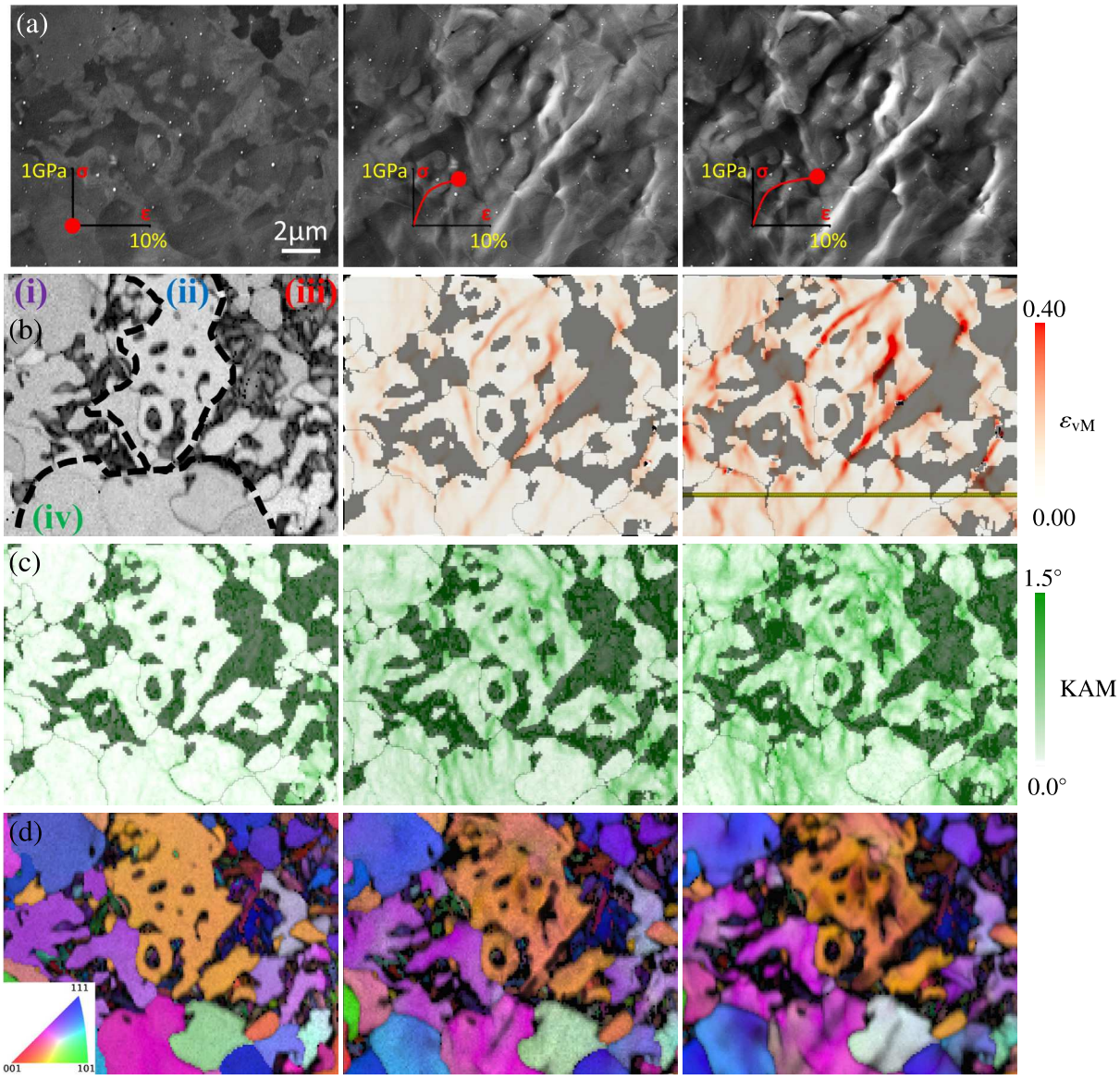

Fig. 4. Results of the *in situ* deformation experiments in the undeformed state (left) and at an average strain of $\bar{\varepsilon}_x = 0.05$ (center) and $\bar{\varepsilon}_x = 0.08$ (right): (a) SE images; (b) μDIC strain maps; (c) EBSD-based kernel average misorientation (KAM) maps; (d) EBSD-based inverse pole figure (IPF) maps. Note that in (a) global stress–strain curves are provided as insets; in (b) the EBSD image quality map of the undeformed stage (left) shows four different regions marked for further discussion in this manuscript and the yellow line indicates location shown in Fig. 5; in (b) and (c) μDICbased strain map is overlayed on EBSD-based ferrite high-angle grain boundary map; and in (d) the inverse pole figure refers to the legend presented in Fig. 2a, and is overlayed to the EBSD-based image quality maps.

misorientation maps indicate the distribution of martensitic-transformation-induced geometrically necessary dislocations (GNDs) [3], and of deformation-induced grain subdivision processes [63]. In the leftmost image in Fig. 4c, the lattice rotation around martensitic regions is clearly observed in the undeformed state, arising due to the volume expansion associated with the martensitic transformation. In some regions with relatively smaller ferrite grain size, almost the full volume of the ferrite grains is affected (see, *e.g.*, lower part of region (iii) and upper right part of region (i)). These ferritic regions which contain a high GND density in the undeformed state, act like the martensitic regions in terms of strain accommodation when deformed, *i.e.* they correspond to low deformation regions that are likely to be avoided by the high strain bands. With further deformation, misorientation gradients are built up within the majority of the ferritic grains, corresponding to deformation-induced grain subdivision [64]. High density of GNDs is expected where there are significant strain gradients. The topmost grain in region (i) is a clear example. The strain map in Fig. 4b reveals that the right half of the grain accommodates significant plastic strain and left half does not. The corresponding KAM distribution in Fig. 4c shows a high value exactly at the section that separates the right half from the left half, indicating a high GND density. Note that some ferritic grains show very

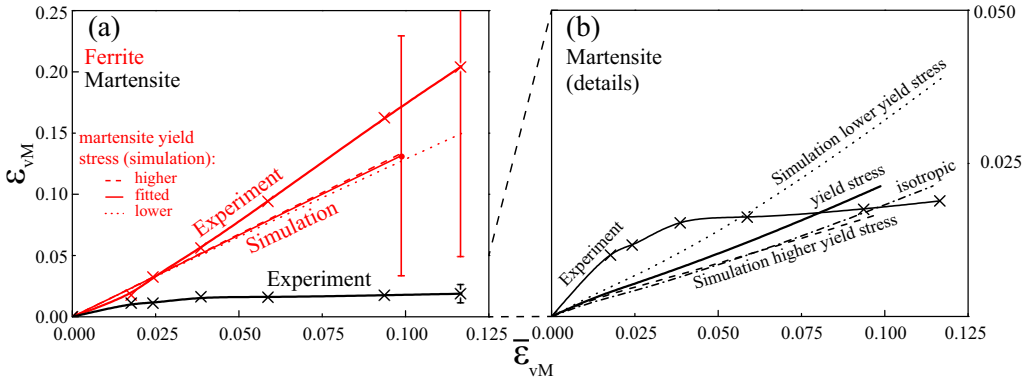

Fig. 5. Comparative analysis of strain partitioning between the experiments (averaged over 50 μDIC data points per phase) and the simulations (averaged over all data points) for: (a) ferrite and (b) martensite. Note that in (a) experimentally obtained martensite is also shown for direct comparison, and in (b), values obtained from different martensite models are shown altogether.

low or almost no increase in local misorientation distribution despite sharp strain bands (see, *e.g.* lower right part of region (iv)). This is due to the maximum misorientation (1.5°) set in calculating the KAM. Higher deformation-induced lattice rotations around the localized strain bands are thus not shown in this map for visual clarity.

In Fig. 4d, inverse pole figure (IPF) maps of the investigated microstructure are presented at different deformation levels. Slight orientation changes are observed in all ferritic grains, while in severely deformed ferrite grains the rotations are more evident, in connection to the associated strain gradients. Note that the presented KAM (Fig. 4c) and IPF (Fig. 4d) maps confirm that high-resolution microstructure mapping can be carried out even in the presence of the μDIC pattern.

For a more quantitative analysis of strain partitioning in the analyzed DP microstructure, the local von Mises strains ε_{vM} accommodated by the martensite and ferrite phases are plotted with respect to the global (average) von Mises strain $\bar{\varepsilon}_{vM}$ in Fig. 5a. Strain evolution in the martensite regions is replotted with different axes in Fig. 5b for better clarity. As expected, the ferrite carries the majority of the deformation, *e.g.* at an average strain $\bar{\varepsilon}_{vM} = 0.10, \varepsilon_{vM} \approx 0.15$ in ferrite compared to $\varepsilon_{vM} \approx 0.02$ in martensite. Comparing the scatter indicated by the vertical bars at the final global deformation level, it can be seen that the strain shows higher heterogeneity in ferrite than in martensite. From Fig. 5b it is interesting to see that a higher rate of straining is recorded for martensite at early stages of deformation, than at later stages (*e.g.* after $\bar{\varepsilon}_{vM} \approx 0.04$).

The evolution of the strain gradients along the section shown in Fig. 4b is plotted in detail in Fig. 6a at different deformation stages for a quantitative analysis of the strain heterogeneity in ferrite. Here it is interesting that (i) sharp strain gradients of up to 0.2 μm^{-1} are developed within ferritic regions, and (ii) the development of the sharp deformation gradient does not lead to macroscopic strain localization. In other words, regions adjacent to a given high deformation band keep on deforming plastically as well, but exhibiting a harder mechanical response. The numerically obtained strain profile is also provided in Fig. 6b, but will be discussed later together with other simulation results.

Following the in situ deformation experiments, serial sectioning is carried out to reveal the microstructure underneath the observed surface layer. This is an important ingredient in the current integrated approach, since the probed microstructures are generally not columnar, *i.e.* micromechanical effects quantified at the surface can be influenced by the microstructure beneath. The results of post-deformation serial sectioning are summarized in Fig. 7.

The BSE images (Fig. 7a) of the as-deformed state (top) and the as-repolished (bottom) state reveal the severe effects of deformation-induced surface roughening. Even upon 1.3 μm repolishing after deformation, the majority of region (ii), which has accommodated significantly more strain compared to the other regions (rightmost image in Fig. 4b), appears dark in the BSE image and thus is not flat Fig. 7a. The undeformed EBSD-based IQ and IPF maps are shown in Fig. 7b and cm respectively, in comparison to the deformed and repolished state. The comparison reveals, except for the non-flat region (ii), whether martensite or ferrite grains extend below the surface. To track certain grains in the third direction, IQ values are considered for distinguishing martensite (see, *e.g.* the three arrows in Fig. 7b), and crystallographic orientations are used for distinguishing different ferrite grains (see, *e.g.* the three arrows in Fig. 7c). This combined analysis reveals that the surface microstructures of regions (i), (ii) and (iv) extend at least 1.3 μm in the depth direction. In contrast, the microstructure in region (iii), *e.g.* the large martensite region shown by the blue arrow in Fig. 7b, is observed to be shallow and has a (soft) ferritic grain underneath.

3.2. Full-field crystal plasticity simulations

Fig. 8 shows simulation results corresponding to the experimental results shown in Figs. 4 and 7 at similar

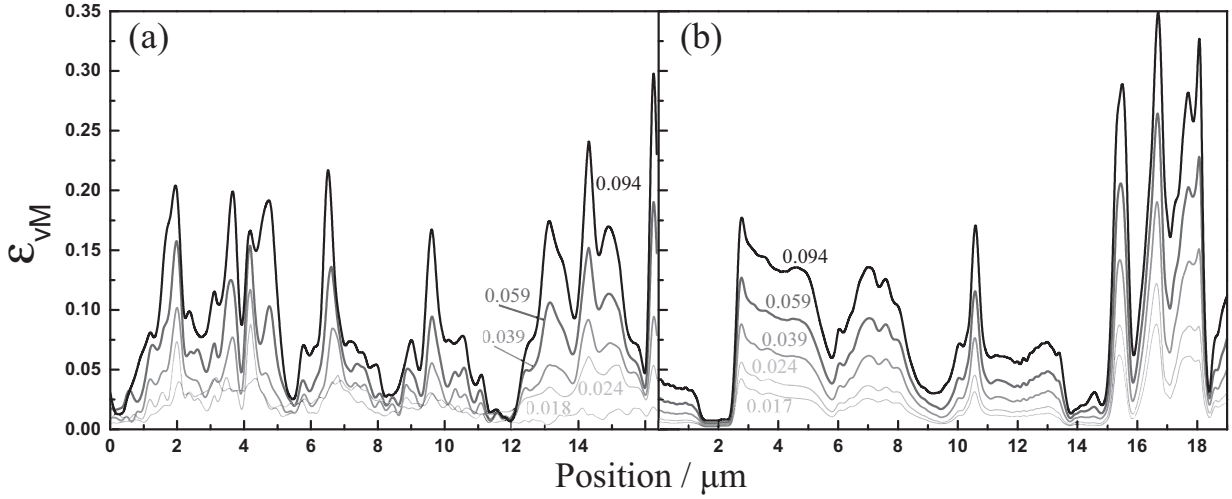

Fig. 6. Profile of the local von Mises strain ε_{vM} along the section shown in Fig. 4b, from (a) experiments, and (b) simulation. Note that the spatial position between (a) and (b) differs slightly.

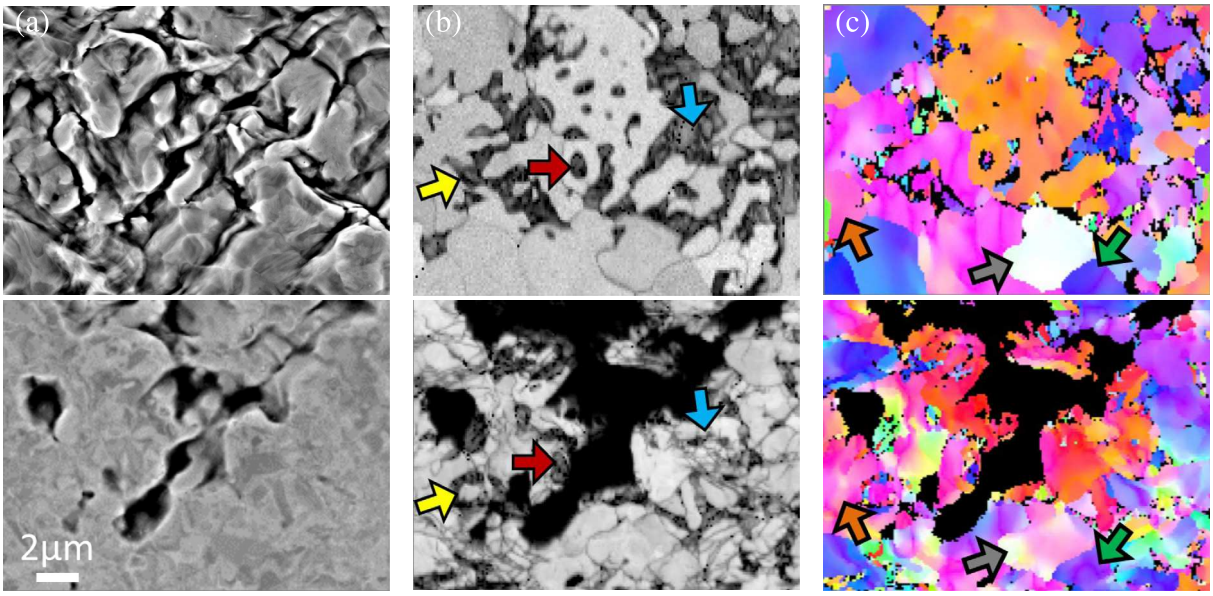

Fig. 7. Results of post-deformation serial sectioning experiments of the as-deformed (top) and as-repolished states (bottom) shown with: (a) BSE images, (b) EBSD-based IQ maps, and (c) EBSD-based IPF maps (legend in Fig. 2). Arrows are placed to track grains. For the repolished state, some deformation topography is still present on the surface (mainly in region (ii)); and that due to the deformation some portions of region (iii) are left out of view.

global deformation steps up to the maximum global strain of $\bar{\varepsilon}_x = 0.08$. Fig. 8 shows the von Mises strain ε_{vM} and stress σ_{vM}, as well as the hydrostatic stress σ' maps.

Comparing the overall strain distributions obtained from the simulations (Fig. 8a) to those from experiments (Fig. 4b) reveals that many features are in good agreement:

- A strong strain partitioning is observed among ferrite and martensite (Fig. 8a, rightmost image), the extent of which is quantitatively assessed in Fig. 5. Comparing the simulation-based ferrite and martensite curves, it can be seen that the ferrite grains accommodate most of the deformation, *i.e.* $\bar{\varepsilon}_{vM} = 0.12 \pm 0.09$ at an average deformation of $\bar{\varepsilon}_{vM} = 0.10$ compared to $\varepsilon_{vM} = 0.02 \pm 0.01$ in martensite. These values correspond well to the experimentally observed strong partitioning shown in the same graph.
- There is also good qualitative agreement in the level of scatter observed in the ferritic regions shown in Fig. 6 for the final deformation level in Fig. 4. The large scatter ($\varepsilon_{vM} = 0.020$–0.35 for a nominal strain of $\varepsilon_{vM} = 0.010$) corresponds to the highly heterogeneous nature of strain distribution in ferrite, which is clearly seen in Figs. 4b and 8a.

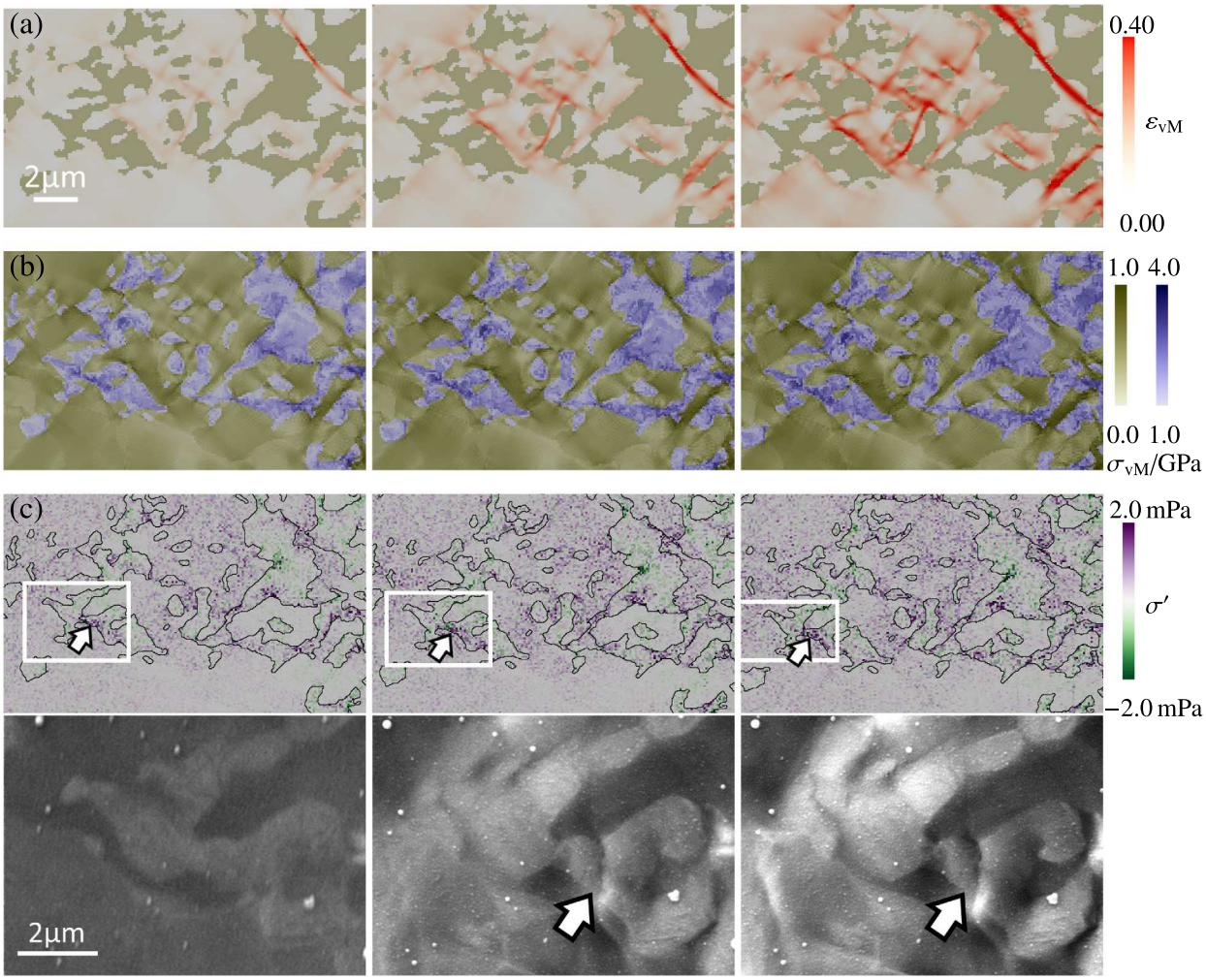

Fig. 8. Numerical results obtained from the CP simulations at an average strain of $\bar{\varepsilon}_x = 0.03$ (left), $\bar{\varepsilon}_x = 0.05$ (center) and $\bar{\varepsilon}_x = 0.08$ (right), showing (a) von Mises strain in ferrite (where gray areas indicate martensite); (b) von Mises stress in ferrite and martensite; (c) hydrostatic stress in ferrite and martensite (top) and SE images showing a damage incident (bottom) taken from Fig. 4a. Arrows indicate the coincidence of high hydrostatic stresses and damage.

- The strain in many ferritic regions is localized in bands oriented at 45°–50° w.r.t. the loading direction in both experiment and simulation.

These observations indicate that the model is suitable to describe the overall mechanical behavior correctly. However, there is an apparent difference between simulation and experiments regarding the exact location of some of the high-strain bands. The possible causes of this difference are analyzed in Section 4.

Given the promising correlation of the local strain from simulations and experiments, stress maps obtained from simulations are considered next (Fig. 8b and c). Focusing on the von Mises stress maps in Fig. 8b, it is observed that long and thin martensite connections aligned with the loading direction experience the highest stress. Interestingly, the local stress peaks up at these points straight away with the start of straining. That is, even at $\bar{\varepsilon}_{vM} = 0.03$, the stress distribution in martensite is very heterogeneous. This pattern is maintained with increasing deformation. Notch effects arising from morphological irregularities also contribute to the high stresses observed in the martensitic areas. The hydrostatic stress is also increased at these notch-like locations. The SE images in Fig. 8c (cropped from region (i) in Fig. 4a) demonstrate that damage nucleation incidents are observed where the hydrostatic stress is locally increased. Interestingly, stress heterogeneity is also observed in martensitic regions where morphology or geometrical orientation do not play significant roles (see, *e.g.* the large martensite grains in region (iii)). It is thus clear that stress in martensite depends on the crystallographic orientation of each block, although this does not reflect a significant difference in strain within such large martensitic regions.

Finally, the influence of martensite constitutive properties on the stress partitioning is presented in Fig. 9 and plotted in Fig. 10 for the profile shown in Fig. 9a. Here it is clearly seen that the martensite in all configurations accommodates most of the stress in the microstructure, having an equivalent stress of $\sigma_{vM} = 1.0$–4.0 MPa compared to $\sigma_{vM} = 0.1$–1.0 MPa in the ferrite. Two trends

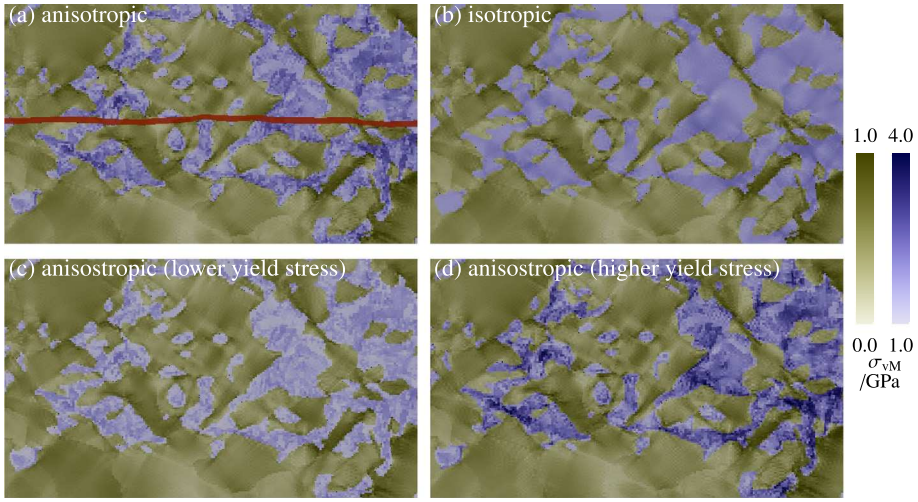

Fig. 9. VON MISES stress distribution shown for differently modeled martensite constitutive response (Table 1b) at an average strain of $\bar{\varepsilon}_x = 0.08$: (a) anisotropic martensite, with default yield behavior. Red line indicates location shown in Fig. 5; (b) isotropic martensite, with default yield behavior; (c) anisotropic martensite with lower yield stress values; (d) anisotropic martensite with higher yield stress values. (For interpretation of the references to colour in this figure legend, the reader is referred to the web version of this article.)

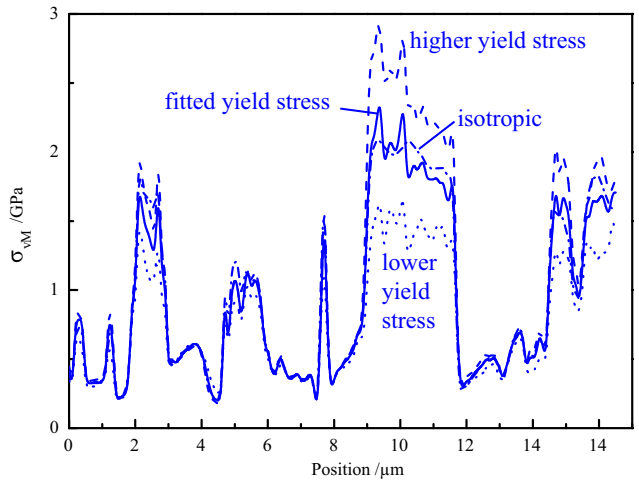

Fig. 10. Simulation-based local VON MISES stress σ_{vM} profile approximately along the section shown in Fig. 4b depending on constitutive parameters chosen for martensite.

are evident: (i) for the martensite with the lower yield stress shown in Fig. 9c, the stress distribution within the martensitic regions is more homogeneous compared to the case with higher martensite yield stress values (Fig. 9d). The effect is more clearly observed in Fig. 10. (ii) Stress heterogeneity in martensite is significantly decreased when the martensite behavior is assumed to be isotropic (cf. Fig. 9a with Fig. 9b).

4. Discussion

The results presented above demonstrate the vast amount of micromechanical data that can be produced by the developed methodology. In this section, the obtained results are discussed in terms of (i) the representativeness of the observed DP micromechanics, and (ii) the understanding thereof gained.

The overall success in capturing the similar qualitative (see Figs. 4b and 8a) and quantitative (see Fig. 5) strain distribution trends in simulations and experiments strongly underlines the representativeness of the presented results. However, differences are observed in some cases as well, e.g. regarding the position of the high strain bands. More specifically, the simulations reveal strain bands that are following narrow ferritic zones in highly martensitic regions (*e.g.* regions (ii) and (iii)), whereas in ferritic regions that are more remote from martensite islands (*e.g.* in region (iv)), the strain distribution is more gradual compared to the experimental results (see Fig. 6a). The causes of these deviations are discussed in the following paragraphs, and tracked to known limitations of the experimental methodology or to the underlying simplifications in the simulation methodology.

The main limitation for the experiments is that SEM is a surface analysis technique and cannot (in a non-destructive manner) be used to reveal 3-D information of the investigated microstructure. This inevitably introduces the columnar microstructure assumption during the model creation process for the simulations, while in reality there may be martensite layers below the surface ferrite grains, or vice versa. However, the post-mortem serial sectioning methodology employed in this work partially compensates for this assumption, by allowing the role of the underlying microstructure to be assessed in a critical manner. An example is discussed regarding region (iii), where a significant difference is observed between experiments and simulations (rightmost images in Figs. 4b, and 8a). The simulations predict a strain band running throughout the gap between two large martensite grains, while in the experiments such a pronounced strain band is not present, and the strain is

much more localized at the narrowest opening between the two martensite grains. Closer inspection of the rightmost image in Fig. 4a reveals that this latter localization point is a continuation of a strain band from region (ii), that "penetrates" the large martensite grain. The serial sectioning data presented in Fig. 7b reveals that this large martensite grain (shown in these micrographs by the blue arrow) is considerably thinner in the z-direction with respect to other martensitic regions in the patch. Thus, the strain band approaching from region (ii) can easily penetrate these large (but thin) martensite regions and cause the unexpected strain localization. This observation obviously cannot be captured in the simulations where the particular martensite grains is considered columnar. Nevertheless, given that only one of the considered four regions have a different subsurface structure (*i.e.* region (iv)), the overall influence on the subsurface microstructure is observed to be limited. This is quantitatively confirmed by the strain-partitioning analysis shown in the results. However, the uncertainty introduced regarding the exact position of localization bands may be enhanced for other microstructures with even finer microstructures.

Regarding the simulations, the effects of (currently not implemented) phenomena such as (i) hardening due to transformation-induced GND densities and (ii) damage nucleation, are also clearly critical in the micromechanical behavior of DP steels. The most obvious examples for the former are observed through the hard response of small ferritic grains with high initial GND density [3] discussed in relation to Fig. 4c. Even though it is clear that the local strain distribution is most strongly dependent on the distribution heterogeneity of martensite (see the strain levels in the identified regions in leftmost image in Fig. 4b), it is revealed in this work that the plastic strain distribution in ferrite is also extremely heterogeneous. Sharp deformation bands nucleate at ferrite grain interiors, and then propagate in the softest routes with 45°–50° angle to the loading direction, even in regions with little or no martensite (*i.e.* region (iv)). These experimental observations of the strong heterogeneity of strain distribution within the ferritic grains (Figs. 4b and 6) suggest that strain gradient effects are significant, and, therefore should be taken into account in future simulations.

An example for the latter phenomena is provided by the microcracking observed in the martensite, in Fig. 8c. Although here only one example is presented on how damage nucleation takes place at unexpectedly low strain levels at narrow sections of the martensite with high hydrostatic stress (rightmost image in Fig. 8c), this is a general phenomenon that plays a significant role in the plasticity of martensite (and the surrounding ferrite). In fact, most martensite grains have such irregular geometries, leading to stress concentrations and early damage nucleation. However, at these low strain levels where damage nucleates, the surrounding ferrite is not yet fully hardened, and thus can successfully arrest these micro-cracks, also effectively dispersing the stress concentration in the process. This effect is believed to be the reason of the discrepancy observed for martensite plasticity at early strain levels (Fig. 5b).

Thus, the discussion on the representativeness of the obtained results can be summarized as follows. The integrated experimental–numerical methodology presented here is able to capture many of the quantitative aspects such as strain and stress partitioning, or heterogeneity, in a realistic way. Further authenticity can be implemented, and full quantitative–qualitative agreement can be achieved when advanced material models are used and if 3-D effects could be successfully taken into account.

Focusing next on DP steel micromechanics, a number of interesting new observations can be discussed. First, as shown in the strain maps in Fig. 4b and the strain profile plot in Fig. 6, the deformation in ferrite in significantly localized. That is, in many ferritic grains sharp strain gradients are captured. This observation is in contrast to some of the earlier works (*e.g.* in Ref. [15]), where more homogeneous strain distributions in ferrite grains were recorded (due to limited spatial resolution). This underlines that the strain partitioning process in martensite–ferrite microstructures differ from that of a conventional composite material with hard–soft components. The soft ferrite phase here has processing-inherited in-grain microstructural heterogeneity, which leads to in-grain heterogeneity of the local mechanical response. Ghassemi-Armaki et al. [65] recently carried out micropillar compression experiments which also demonstrate this form of mechanical heterogeneity in ferritic grains. Various causes can be proposed for such heterogeneity, *e.g.* dislocation density gradients due to transformation-induced GNDs, transformation-induced residual stresses, ferrite grain size heterogeneity, martensite autotempering-induced carbon pipe diffusion into accommodation dislocations in ferrite, etc., all leading to the same micromechanical behavior: The deformation of the relatively harder shell of a given ferritic grain is further constrained due to the surrounding hard martensite, allowing the ferritic core to accommodate most of the plastic deformation, and causing the observed sharp strain bands. From an alloy design point of view, this result indicates that the ferrite properties are as important as those of martensite in the design of DP steels with optimal mechanical behavior.

The second interesting point regards the early stress peaking, plastic deformation and damage nucleation in preferential martensitic sites, see Figs. 8b, 5 and 8c, respectively. Regarding this observation, the CP simulations suggest that the shape of the martensite and its local alignment with respect to the loading direction play a direct role Fig. 8b. This analysis is supported by earlier experimental reports that show that high martensite plasticity and damage resistance can be achieved when martensite morphology is, for example, spherical [3].

Simulations with different martensite behavior reveal another interesting observation regarding the micromechanics of DP steels (see Fig. 9, as well as Fig. 5). Appar-

ently, the behavior of the martensite has only a small influence on the stress–strain partitioning in the microstructure (simulation results for ferrite in Fig. 5a and for martensite in Fig. 5b). Alteration of martensite properties has a more pronounced effect on the heterogeneity of stress distribution inside the martensitic regions (Fig. 9). For example, for the harder martensite shown in Fig. 9d, relatively higher stress levels are observed within the narrow zones aligned parallel to the loading direction, compared to small, isolated martensitic islands. This observation again clearly underlines the importance of martensite shape and morphology in DP steel micromechanics. Thus, avoiding early damage nucleation in martensite, especially when martensite carbon content is high, requires avoiding morphological irregularities that give rise to stress intensification effects.

5. Conclusions

A novel integrated experimental–numerical methodology is proposed that allows the analysis of strain and stress partitioning in complex multiphase materials. This methodology includes a number of improvements with respect to previous efforts in terms of the complexity of the microstructure handled, the resolution at which the microstructure and deformation is tracked, the fidelity with which the microstructure is mapped and modeled, and particularly the interplay between the experiments and the simulations. As a proof-of-principle this novel integrative approach is applied here to the case study of a DP steel. The analysis revealed that:

- Concurrent strain and microstructure mapping can be achieved to the point of damage nucleation, at high resolution and field-of-view, by the recently developed in situ testing method.
- Physically based microstructure models can be created, and the corresponding crystal plasticity problems numerically solved, using the DAMASK framework and the recently developed advanced spectral method suitable for heterogeneous material behavior.
- Given the known complexity of the micromechanics of DP microstructures, the proof-of-principle study of DP steel reveals good agreement between the results obtained from experiments and simulations.
- Inconsistencies between the experiments and simulations can be tracked back to known limitations in the experimental and numerical methodologies, such as 3-D effects for the former, and damage and strain-gradient effects for the latter.
- Regarding micromechanics of DP steels, the importance of martensite morphology is observed to be critical, especially for harder (*i.e.* high-carbon) martensite.
- Unexpected strain heterogeneity is observed in the ferrite, which relates to the in-grain microstructural heterogeneities arising from the processing.

Acknowledgments

Parts of this research were carried out under project number M 41.2.10410 in the framework of the research program of the materials innovation institute M2i (www.m2i.nl). The material model implementation was performed as part of the "Computational Mechanics of Polycrystals—CMC^n" initiative. The funding by the European Research Council under the EU's 7th Framework Programme (FP7/2007-2013)/ERC Grant agreement 290998 is gratefully acknowledged. The financial support from the International Max Planck Research School for Surface and Interface Engineering in Advanced Materials (IMPRS-SurMat) is also gratefully acknowledged.

Appendix A. Constitutive models

A.1. Phenomenological crystal plasticity model

The formulation is an adoption for body-centered cubic (bcc) crystals of the phenomenological CP description by Peirce et al. [51]. The microstructure is parameterized in terms of a slip resistance $s^{\alpha}_{\{0\,1\,1\}}$ on each of the 12 $\{0\,1\,1\}\langle 1\,1\,1\rangle$ slip systems, and $s^{\alpha}_{\{2\,1\,1\}}$ on each of the 12 $\{2\,1\,1\}\langle 1\,1\,1\rangle$ slip systems which are indexed by $\alpha = 1,\ldots,24$. These resistances increase asymptotically towards s^{α}_{∞} with shear γ according to the relationship

$$\dot{s}^{\alpha} = h_0\left(1 - s^{\alpha}/s^{\alpha}_{\infty}\right)^{w} h_{\alpha\beta}\ \dot{\gamma}^{\beta} \tag{1}$$

with interaction $(h_{\alpha\beta})$ and fitting (w, h_0) parameters. Given a set of current slip resistances, shear on each system evolves at a rate of

$$\dot{\gamma}^{\alpha} = \dot{\gamma}_0 \left|\frac{\tau^{\alpha}}{s^{\alpha}}\right|^{n} \operatorname{sgn}(\tau^{\alpha}), \tag{2}$$

with $\tau^{\alpha} = \mathbf{S}\cdot(\mathbf{b}^{\alpha}\otimes\mathbf{n}^{\alpha})$, a reference shear rate $\dot{\gamma}_0$ and a stress exponent n. The superposition of shear on all slip systems in turn determines the plastic velocity gradient:

$$\mathbf{L}_{\mathrm{p}} = \dot{\gamma}^{\alpha}\ \mathbf{b}^{\alpha}\otimes\mathbf{n}^{\alpha}, \tag{3}$$

where $\mathbf{b}^{\alpha}$ and $\mathbf{n}^{\alpha}$ are unit vectors along the slip direction and slip plane normal, respectively.

A.2. Isotropic von Mises plasticity

An isotropic simplification of the CP constitutive law assumes that the second invariant J_2 of the stress deviator $\mathbf{S}^{*} = \operatorname{dev}\mathbf{S}$ is driving dislocation motion. Plastic shear occurs at the rate:

$$\dot{\gamma} = \dot{\gamma}_0\left(\frac{\sqrt{3J_2}}{M\ g}\right)^{n} = \dot{\gamma}_0\left(\sqrt{\frac{3}{2}}\ \frac{\|\mathbf{S}^{*}\|_{\mathrm{F}}}{M\ g}\right)^{n} \tag{4}$$

with $\dot{\gamma}_0$ a reference shear rate, n the stress exponent, and M an orientation (Taylor) factor. The resistance to plastic flow, g, evolves asymptotically towards g_{∞} with plastic shear γ according to the relationship:

$$\dot{g} = \dot{\gamma}\ h_0 |1 - g/g_\infty|^a\ \mathrm{sgn}(1 - g/g_\infty) \tag{5}$$

with parameters h_0 and a. The plastic velocity gradient $\mathbf{L}_\mathrm{p}$ scales with the rate of shear and its "direction" is set equivalent to that of $\mathbf{S}^*$:

$$\mathbf{L}_\mathrm{p} = \frac{\dot{\gamma}}{M}\ \frac{\mathbf{S}^*}{\|\mathbf{S}^*\|_\mathrm{F}}. \tag{6}$$

Appendix B. The spectral method based boundary value solver

$\mathcal{B}_0 \subset \mathbb{R}^3$ is an hexahedral microstructural domain with periodic boundary conditions on which an average deformation gradient $\overline{\mathbf{F}}$ is imposed. The resulting deformation defines a field $\boldsymbol{\chi}(\mathbf{x}) : \mathbf{x} \in \mathcal{B}_0 \rightarrow \mathbf{y} \in \mathcal{B}$ which can be decomposed as the sum of a locally fluctuating displacement field $\tilde{\mathbf{w}}$ and the imposed average displacement:

$$\boldsymbol{\chi}(\mathbf{x}) = \overline{\mathbf{F}}\mathbf{x} + \tilde{\mathbf{w}}(\mathbf{x}), \tag{7}$$

The total deformation gradient, given by $\mathbf{F} = \partial\boldsymbol{\chi}/\partial\mathbf{x} = \boldsymbol{\chi} \otimes \nabla = \mathrm{Grad}\boldsymbol{\chi}$, can similarly be decomposed as the sum of the imposed macroscopic deformation gradient, $\overline{\mathbf{F}}$, and the locally fluctuating displacement gradient, $\widetilde{\mathbf{F}}$:

$$\mathbf{F} = \overline{\mathbf{F}} + \widetilde{\mathbf{F}} \quad \text{with } \widetilde{\mathbf{F}} = \frac{\partial\tilde{\mathbf{w}}}{\partial\mathbf{x}} = \tilde{\mathbf{w}} \otimes \nabla = \mathrm{Grad}\tilde{\mathbf{w}}. \tag{8}$$

The constitutive response of the material relates the deformation gradient to the first Piola–Kirchhoff stress, $\mathbf{P}$, through a strain energy density functional, $\mathcal{W}$:

$$\mathbf{P}(\mathbf{x}) = \frac{\delta\mathcal{W}}{\delta\mathbf{F}(\mathbf{x})}, \tag{9}$$

The static equilibrium deformation field is obtained by minimizing $\mathcal{W}$ over all admissible deformation fields and reads (in real and Fourier[1] space):

$$\min_{\boldsymbol{\chi}} \mathcal{W} \Rightarrow \mathrm{Div}\mathbf{P}(\mathbf{x}) = \mathcal{F}^{-1}[\mathbf{P}(\mathbf{k})\ i\ \mathbf{k}] = \mathbf{0}, \tag{10}$$

which is equivalent to finding the nonlinear root of the residual body force field

$$\widehat{\mathcal{F}}[\boldsymbol{\chi}(\mathbf{k})] := \mathbf{P}(\mathbf{k})\ i\mathbf{k} = \mathbf{0}. \tag{11}$$

Since Eq. (11) is difficult to solve numerically, a related problem in a linear homogeneous reference material of stiffness $\mathbb{A}$ (*i.e.* $\mathbf{P}(\mathbf{x}) = \mathbb{A}\mathbf{F}(\mathbf{x}) = \mathbb{A}\mathrm{Grad}\boldsymbol{\chi}$) is considered. Equilibrium in this reference material is fulfilled if, for a given deformation map $\boldsymbol{\chi}$, the residual body force field vanishes:

$$\widehat{\mathcal{P}}[\boldsymbol{\chi}(\mathbf{k})] := \mathbb{A}[\boldsymbol{\chi}(\mathbf{k}) \otimes i\ \mathbf{k}]\ i\ \mathbf{k} = \mathbf{A}(\mathbf{k})\ \boldsymbol{\chi}(\mathbf{k}) = \mathbf{0}. \tag{12}$$

The acoustic tensor $\mathbf{A}(\mathbf{k})$ is defined such that $\mathbf{A}(\mathbf{k})\ \mathbf{a}(\mathbf{k}) = \mathbb{A}[\mathbf{a}(\mathbf{k}) \otimes\ i\ \mathbf{k}]\ i\ \mathbf{k}$ for any vector field $\mathbf{a}(\mathbf{k})$. The inverse $\mathbf{A}^{-1}$ gives the deformation map that corresponds to a known body force field in the reference material. This deformation map vanishes iff the body force field vanishes, *i.e.*, in static equilibrium, since $\mathbf{A}(\mathbf{k})$ is non-zero $\forall\ \mathbf{k} \neq \mathbf{0}$ and for positive-definite stiffness $\mathbb{A}$. Motivated by this, we define an operator that results in the deformation map causing the same body force field in the reference material as a given deformation map in the original material. Mathematically this corresponds to a preconditioning operation of $\widehat{\mathcal{P}}^{-1}$ on the nonlinear operator $\widehat{\mathcal{F}}$. $\widehat{\mathcal{P}}$ is straightforward to invert since it is local in $\mathbf{k}$, with $\widehat{\mathcal{P}}^{-1} = \mathbf{A}(\mathbf{k})^{-1}$. The preconditioned system thus reads:

$$\widehat{\mathcal{P}}^{-1}\widehat{\mathcal{F}}[\boldsymbol{\chi}(\mathbf{k})] = \mathbf{A}(\mathbf{k})^{-1}\mathbf{P}(\mathbf{k})\ i\ \mathbf{k} = \mathbf{0} \quad \forall\ \mathbf{k} \neq \mathbf{0}. \tag{13}$$

The deformation gradient field corresponding to this deformation map is obtained from the gradient in real space of Eq. (13)

$$\widehat{\mathcal{P}}^{-1}\widehat{\mathcal{F}}[\boldsymbol{\chi}(\mathbf{k})] \otimes i\ \mathbf{k} = [\mathbf{A}(\mathbf{k})^{-1}\mathbf{P}(\mathbf{k})\ i\ \mathbf{k}] \otimes i\ \mathbf{k} = \mathbf{0} \quad \forall\ \mathbf{k} \neq \mathbf{0}. \tag{14}$$

This is equivalent to Eq. (13) up to a constant residual field, *i.e.* at $\mathbf{k} = \mathbf{0}$. Expressed in terms of the deformation gradient field Eq. (14) reads:

$$\widehat{\mathcal{F}}[\mathbf{F}(\mathbf{k})] := \mathbb{\Gamma}(\mathbf{k})\ \mathbf{P}(\mathbf{k}) = \mathbf{0} \quad \forall\ \mathbf{k} \neq \mathbf{0}, \tag{15}$$

where the "Gamma operator" $\mathbb{\Gamma}(\mathbf{k})$ is defined such that $\mathbb{\Gamma}(\mathbf{k})\ \mathbf{T}(\mathbf{k}) = [\mathbf{A}(\mathbf{k})^{-1}\mathbf{T}(\mathbf{k})\ i\ \mathbf{k}] \otimes i\ \mathbf{k}$.

A collocation-based approach at the grid points is used to discretize the basic variational form of the static equilibrium condition (Eq. (15)) in real space into a regular grid of $N_x \times N_y \times 1 = N$ points and the solution field is approximated in the discrete Fourier space associated with this grid. The resulting system of equations reads:

$$\mathcal{F}[\mathbf{F}(\mathbf{x})] := \mathcal{F}^{-1}\begin{pmatrix} \mathbb{\Gamma}(\mathbf{k})\ \mathbf{P}(\mathbf{k}) & \text{if } \mathbf{k} \neq \mathbf{0} \\ \Delta\mathbf{F}_\mathrm{BC} & \text{if } \mathbf{k} = \mathbf{0} \end{pmatrix} \tag{16}$$

where $\Delta\mathbf{F}_\mathrm{BC}$ is the change in pure deformation gradient boundary condition required to enforce mixed boundary conditions.

Appendix C. Notation

As a general scheme of notation, vectors are written as boldface lowercase letters (*e.g.* $\mathbf{a}, \mathbf{b}$), second-order tensors as boldface capital letters (*e.g.* $\mathbf{A}, \mathbf{B}$), and fourth-order tensors as blackboard-bold capital letters (*e.g.* $\mathbb{A}, \mathbb{B}$). For vectors and tensors, Cartesian components are denoted as, respectively, a_i, A_{ij} and A_{ijkl}. The action of a second-order tensor upon a vector is denoted as $\mathbf{Ab}$ (in components $A_{ij}b_j$, implicit summation is repeated unless specified otherwise) and that of a fourth-order tensor upon a second-order tensor is designated as $\mathbb{A}\mathbf{B}$ ($A_{ijkl}B_{kl}$). The composition of two second-order tensors is denoted as $\mathbf{AB}$ ($A_{ik}B_{kj}$). The tensor (or dyadic) product between two vectors is denoted

[1] Quantities in real space and Fourier space are distinguished by notation $Q(\mathbf{x})$ and $Q(\mathbf{k})$, respectively, with $\mathbf{x}$ the position in real space, $\mathbf{k}$ the frequency vector in Fourier space, and $i^2 = -1$. $\mathcal{F}^{-1}$ denotes inverse Fourier transform.

as $\mathbf{a} \otimes \mathbf{b}$ ($a_i b_j$). All inner products are indicated by a single dot between the tensorial quantities of the same order, *e.g.*, $\mathbf{a} \cdot \mathbf{b}$ ($a_i b_i$) for vectors and $\mathbf{A} \cdot \mathbf{B}$ ($A_{ij} B_{ij}$) for second-order tensors. $\|\mathbf{A}\|_F$ designates the FROBENIUS norm of matrix $\mathbf{A}$. The "del" operator is denoted by the symbol nabla ∇.

References

[1] Gutierrez-Urrutia I, Raabe D. Acta Mater 2011;59:6449.
[2] Rashid MS. Ann Rev Mater Sci 1981;11:245.
[3] Calcagnotto M, Adachi Y, Ponge D, Raabe D. Acta Mater 2011;59:658.
[4] Davut K, Zaefferer S. Steel Res Int 2012;83:584.
[5] De Cooman BC. Curr Opin Solid State Mater Sci 2004;8:285.
[6] Seshacharyulu T, Medeiros SC, Frazier WG, Prasad YVRK. Mater Sci Eng A 2002;325:112.
[7] Lütjering G. Mater Sci Eng A 1998;243:32.
[8] Bieler TR, Eisenlohr P, Roters F, Kumar D, Mason DE, Crimp MA, et al. Int J Plast 2009;25:1655.
[9] Kang J, Ososkov Y, Embury J, Wilkinson D. Scr Mater 2007;56:999.
[10] Yan D, Tasan CC, Raabe D. Acta Mater, submitted for publication.
[11] Ghadbeigi H, Pinna C, Celotto S, Yates JR. Mater Sci Eng A 2010;527:5026.
[12] Kapp M, Hebesberger T, Kolednik O. Int J Mater Res 2011;102:687.
[13] Joo SH, Lee JK, Koo JM, Lee S, Suh DW, Kim HS. Scr Mater 2013;68:245.
[14] Han Q, Kang Y, Hodgson PD, Stanford N. Scr Mater 2013;69:13.
[15] Tasan CC, Hoefnagels JPM, Geers MGD. Scr Mater 2010;62:835.
[16] Shen HP, Lei TC, Liu JZ. Mater Sci Technol 1986;2:28.
[17] Tarigopula V, Hopperstad O, Langseth M, Clausen A. Eur J Mech A/Solids 2008;27:764.
[18] Morgeneyer TF, Taillandier-Thomas T, Helfen L, Baumbach T, Sinclair I, Roux S, et al. Acta Mater 2014;69:78.
[19] Choi KS, Liu WN, Sun X, Khaleel MA. Metal Mater Trans A 2009;40:796.
[20] Liedl U, Traint S, Werner E. Comput Mater Sci 2002;25:122.
[21] Al-Abbasi FM, Nemes J. Int J Mech Sci 2003;45:1449.
[22] Al-Abbasi FM, Nemes J. Comput Mater Sci 2007;39:402.
[23] Thomser C. Modelling of the mechanical properties of dual phase steels based on microstructure [Ph.D. thesis]. Aachen; 2009.
[24] Tarigopula V, Hopperstad O, Langseth M, Clausen A, Hild F. Int J Solids Struct 2008;45:601.
[25] Mazinani M, Poole WJ. Metal Mater Trans A 2007;38:328.
[26] Marteau J, Haddadi H, Bouvier S. Exp Mech 2013;53:427.
[27] Martin G, Sinclair CW, Schmitt JH. Scr Mater 2013;68:695.
[28] Kadkhodapour J, Schmauder S, Raabe D, Ziaei-Rad S, Weber U, Calcagnotto M. Acta Mater 2011;59:4387.
[29] Delaire F, Raphanel JL, Rey C. Acta Mater 2000;48:1075.
[30] Raabe D, Sachtleber M, Zhao Z, Roters F, Zaefferer S. Acta Mater 2001;49:3433.
[31] Zhao Z, Ramesh M, Raabe D, Cuitiño AM, Radovitzky R. Int J Plast 2008;24:2278.
[32] Cédat D, Fandeur O, Rey C, Raabe D. Acta Mater 2012;60:1623.
[33] Sun X, Choi KS, Soulami A, Liu WN, Khaleel MA. Mater Sci Eng A 2009;526:140.
[34] Sun X, Choi KS, Liu WN, Khaleel MA. Int J Plast 2009;25:1888.
[35] Wang L, Barabash RI, Yang Y, Bieler TR, Crimp MA, Eisenlohr P, et al. Metal Mater Trans A 2011;42:626.
[36] Choi SH, Kim EY, Woo W, Han SH, Kwak JH. Int J Plast 2013;45:85.
[37] Pokharel R, Lind J, Kanjarla AK, Lebensohn RA, Li SF, Kenesei P, et al. Ann Rev Condens Matter Phys 2014;5:317.
[38] Knezevic M, Lebensohn RA, Cazacu O, Revil-Baudard B, Proust G, Vogel SC, et al. Mater Sci Eng A 2013;564:116.
[39] Lim H, Carroll JD, Battaile CC, Buchheit TE, Boyce BL, Weinberger CR. Int J Plast 2014;60:1.
[40] Martin G, Sinclair CW, Lebensohn RA. Mater Sci Eng A 2014;603:37.
[41] Gutierrez-Urrutia I, Zaefferer S, Raabe D. JOM 2013;65:1229.
[42] Zambaldi C, Raabe D. Acta Mater 2010;58:3516.
[43] Yang Y, Wang L, Zambaldi C, Eisenlohr P, Barabash R, Liu W, et al. JOM 2011;63:66.
[44] Eisenlohr P, Diehl M, Lebensohn RA, Roters F. Int J Plast 2013;46:37.
[45] Shanthraj P, Eisenlohr P, Diehl M, Roters F, Int J Plast, in press.
[46] Tasan CC, Hoefnagels JPM, Diehl M, Yan D, Roters F, Raabe D, Int J Plast, in press.
[47] Raabe D, Sachtleber M, Weiland H, Scheele G, Zhao Z. Acta Mater 2003;51:1539.
[48] Ma A, Roters F. Acta Mater 2004;52:3603.
[49] Roters F, Eisenlohr P, Kords C, Tjahjanto DD, Diehl M, Raabe D. In: Cazacu O, editor. Procedia IUTAM: IUTAM symposium on linking scales in computation: from microstructure to macroscale properties, vol. 3. Amsterdam: Elsevier; 2012. p. 3–10.
[50] DAMASK. Düsseldorf advanced material simulation kit; 2014.
[51] Peirce D, Asaro RJ, Needleman A. Acta Metal 1982;30:1087.
[52] Steinmetz DR, Jäpel T, Wietbrock B, Eisenlohr P, Gutierrez-Urrutia I, Saeed-Akbari A, et al. Acta Mater 2013;61:494.
[53] Reuber C, Eisenlohr P, Roters F, Raabe D. Acta Mater 2014;71:333.
[54] Roters F, Eisenlohr P, Hantcherli L, Tjahjanto DD, Bieler TR, Raabe D. Acta Mater 2010;58:1152.
[55] Moulinec H, Suquet P. C R Acad Sci Paris Ser II 1994;318:1417.
[56] Moulinec H, Suquet P. Comput Methods Appl Mech Eng 1998;157:69.
[57] Montagnat M, Blackford JR, Piazolo S, Arnaud L, Lebensohn RA. Earth Planet Sci Lett 2011;305:153.
[58] Lee SB, Lebensohn RA, Rollett AD. Int J Plast 2011;27:707.
[59] Lebensohn RA, Rollett AD, Suquet P. JOM 2011;63:13.
[60] Kanjarla AK, Lebensohn RA, Balogh L, Tomé CN. Acta Mater 2012;60:3094.
[61] Zambaldi C, Yang Y, Bieler TR, Raabe D. J Mater Res 2012;27:356.
[62] Tjahjanto DD, Turteltaub S, Suiker ASJ. Contin Mech Thermodyn 2008;19:399.
[63] Allain-Bonasso N, Wagner F, Berbenni S, Field DP. Mater Sci Eng A 2012;548:56.
[64] Raabe D, Zhao Z, Park SJ, Roters F. Acta Mater 2002;50:421.
[65] Ghassemi-Armaki H, Chen P, Bhat S, Sadagopan S, Kumar S, Bower A. Acta Mater 2013;61:3640.